Check for updates

Lithospheric electrical structure across the Bangong-Nujiang Suture in northern tibet revealed by magnetotelluric

Zhen Yang[1], Hongda Liang[2,3]*, Rui Gao[1,3,4], Jiangtao Han[5], Zhonghua Xin[5], Jianqiang Kang[5], Zhuoxuan Shi[1], Lu Zhang[1], Rui Qi[6] and Huilin Li[1]

[1]School of Earth Science and Engineering, Sun Yat-Sen University, Zhuhai, Guangdong, China, [2]Institute of Geophysical and Geochemical Exploration, Chinese Academy of Geological Science, Langfang, Hebei, China, [3]Southern Marine Science and Engineering Guangdong Laboratory (Zhuhai), Zhuhai, Guangdong, China, [4]Key Laboratory of Deep-Earth Dynamics of Ministry of Natural Resources, Institute of Geology, Chinese Academy of Geological Sciences, Beijing, China, [5]College of Geoexploration Science and Technology, Jilin University, Changchun, China, [6]Department of Mathematical Sciences, Tsinghua University, Beijing, China

Competing hypotheses have been proposed to explain the subduction polarity of the Bangong-Nujiang Tethyan Ocean and the formation of the high-conductivity anomaly beneath the Qiangtang terrane. However, the lithospheric architecture of the northern Tibetan Plateau is still poorly understood due to inhospitable environments and topography. Therefore, in the winter of 2021, a 440 km long, SN-trending broadband magnetotelluric (MT) profile was recorded in northern Tibet to detect its regional lithospheric structure. The nonlinear conjugate gradients algorithm is conducted to invert the individual TM mode data. A reliable 2D electrical model was obtained by ablation processing and analysis of broadband magnetotelluric data to test the lithospheric electrical structure and dynamics between the northern Lhasa and Qiangtang terranes. The inversion results reveal the lithospheric structure at a depth of 100 km in northern Tibet, which synthesizes geological, geochemical and deep seismic reflection evidence and firmly identifies that the trace of the south-dipping conductor mainly resulted from the southward subduction of the Bangong-Nujiang Tethyan Ocean under the Lhasa terrane and the trace of the north-dipping conductor likely due to the northward subduction of the Bangong-Nujiang Tethyan Ocean under the Qiangtang terrane. In addition, the magnetotelluric profile also images a high-conductivity lithospheric-scale anticline beneath the central Qiangtang terrane, which may correspond to the upwelling of postcollisional magmatism triggered by northward subduction of the Bangong-Nujiang Tethyan Ocean under the Qiangtang terrane, aqueous fluid and/or partial melting.

1 Introduction

The Tibetan Plateau, which lies in the region of continental-continental convergence between the Indian and Eurasian plates in the Cenozoic, has been an orogenic belt with the highest elevation and the youngest orogeny history in the world. The region is also a natural field laboratory for global dynamics. It has become a window for the discussion of basic geodynamic problems such as plate convergence, continental collision, intracontinental subduction and large-scale surface uplift (Gao et al., 2013). From north to south, the Himalaya-Tibetan Plateau is assembled mainly by four terranes, that is, the Songpan-Ganzi terrane, Qiangtang terrane, Lhasa terrane and the Tethys-Himalaya terrane, and these terranes are separated from each other by Jinsha River suture (JRS), Bangong-Nujiang suture (BNS) and Indus-Yarlung Zangbo suture (IYS) (Zhu et al., 2013, 2016) (Figure 1A).

The Bangong-Nujiang suture zone (BNS) is located between the Lhasa terrane (LS) in the south and Qiangtang terrane (QT) in the north and is broadly overlain by ancient magmatic rocks and discontinuous ophiolitic fragments (Yin and Harrison, 2000; Kapp et al., 2007; Peng et al., 2020) related to the subduction and demise of the Bangong-Nujiang Tethyan Ocean (BTO) between the Late Jurassic and Early Cretaceous (Yin and Harrison, 2000). However, the subduction polarity of the BTO remains under abundant debate, of which bidirectional subduction, northward subduction, and southward subduction are prevailing views (Yin and Harrison, 2000; Kapp and DeCelles, 2019). The first hypothesis is northward subduction beneath the Qiangtang terrane (Yin and Harrison, 2000; Fan et al., 2015; Li et al., 2017). The second hypothesis is that some studies supported the southward subduction of the BTO under the Lhasa terrane (Kang et al., 2010; Zhu et al., 2013). The third hypothesis is that some researchers have speculated on the bidirectional subduction of the BTO, including southward subduction under the Lhasa terrane and northward subduction under the Qiangtang terrane (Zhu et al., 2016; Li et al., 2018; Shi et al., 2021; Ding et al., 2022).

The Qiangtang terrane is located in the northern Tibetan Plateau, sandwiched between the Songpan-Ganzi terrane in the north and the Lhasa terrane in the south, bounded by Jinsha River suture in the north and Bangong-Nujiang suture in the south, with the Altun strike-slip fault zone in the west and the north Lancang River fault zone in the east, and it is a large-scale anticlinorium with blueschist-bearing mélange in the core and Jurassic sedimentary rocks along the limbs (Pullen et al., 2008; Zhu et al., 2013). The Longmu Tso-Shuanghu fault (LSF) in the central Qiangtang terrane divides the Qiangtang terrane into two subterranes, the southern Qiangtang basin and the northern Qiangtang basin (Zhang et al., 2016a; Zhu et al., 2016), which is characterized by Jurassic marine sediments and is also called the central Qiangtang metamorphic belt (comprising blueschist and eclogite). Recently, increasing evidence indicates that the
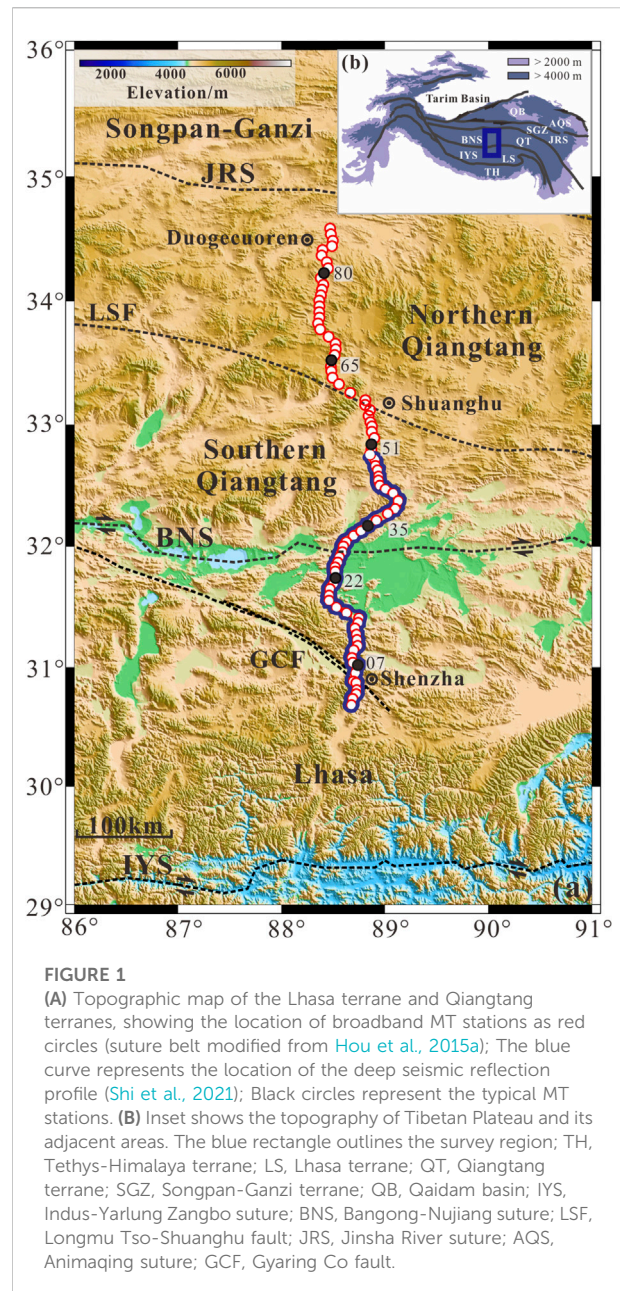
FIGURE 1
(A) Topographic map of the Lhasa terrane and Qiangtang terranes, showing the location of broadband MT stations as red circles (suture belt modified from Hou et al., 2015a); The blue curve represents the location of the deep seismic reflection profile (Shi et al., 2021); Black circles represent the typical MT stations. **(B)** Inset shows the topography of Tibetan Plateau and its adjacent areas. The blue rectangle outlines the survey region; TH, Tethys-Himalaya terrane; LS, Lhasa terrane; QT, Qiangtang terrane; SGZ, Songpan-Ganzi terrane; QB, Qaidam basin; IYS, Indus-Yarlung Zangbo suture; BNS, Bangong-Nujiang suture; LSF, Longmu Tso-Shuanghu fault; JRS, Jinsha River suture; AQS, Animaqing suture; GCF, Gyaring Co fault.

Qiangtang terrane shows a high-conductivity anomaly (Zeng et al., 2015; Sheng et al., 2019), SKS anisotropy (Huang et al., 2000), and widespread distribution of volcanism (Yin and Harrison, 2000). Therefore, understanding the deep structure of the Qiangtang terrane is essential to determine the tectonic evolution of the Qiangtang terrane and the Tibetan Plateau.

To date, a variety of geophysical studies have been carried out in the Lhasa and Qiangtang terranes, mainly including gravity and magnetism (He et al., 2014) and magnetotellurics (Wei et al., 2001; Unsworth et al., 2005; Zeng et al., 2015; Liang et al., 2018; Sheng et al., 2019; Xue et al., 2021; Jin et al., 2022). Deep seismic

reflection detection (Ross et al., 2004; Gao et al., 2013, 2016; Lu et al., 2015; Shi et al., 2021) and seismological methods (He et al., 2010; Xu et al., 2011; Shi et al., 2016) have provided essential information for the convergent front of Indian lithosphere, high-conductivity and low-velocity material inside the crust.

In general, previous geophysical studies have mainly focused on the direct contact zone of continent-continent collisions in the southern Tibetan Plateau. In addition, the Qiangtang terrane has never been fully imaged due to the limitations of the survey conditions. Accordingly, to provide fresh insights into the subduction polarity of the Bangong-Nujiang Tethyan Ocean and the formation of a high-conductivity anomaly underneath the Qiangtang terrane, in the winter of 2021, an MT profile passing through the northern Lhasa terrane and Qiangtang terrane was deployed to detect the deep electrical structure in the northern Tibetan Plateau.

2 Data and inversion

2.1. Data acquisition and processing

The field magnetotelluric data were taken at the time of 2021, and the red circles in Figure 1A indicate the location of the magnetotelluric measurement point. The measurement line consisted of a south-north-oriented profile that started from Shenzha County in the Lhasa terrane and terminated in Duogecuoren in the Qiangtang terrane (Figure 1A). The SN-trending MT profile extends northward through the Gyaring co fault, the Bangong-Nujiang suture, and the Longmu Tso-Shuanghu fault, with a total length of approximately 440 km. A total of 86 broadband magnetotelluric (BBMT) measurement points were conducted at an ~5-km spacing along the profile. The MTU-5A broadband magnetotelluric instrument from Canada's Phoenix Geophysics was used for field data acquisition. The three time-varying magnetic field components (Hx, Hy and Hz; x, y, and z are the south-north, east-west and vertical directions) and two orthogonal electric field components (Ex and Ey) were recorded by commercial instruments. To effectively suppress noise interference and improve the signal-to-noise ratio of the data, the average recording time of each measurement point was longer than 20 h, and the measurements were acquired over a period range of 0.003–2000 s. Additionally, the MT sites are collected using GPS simultaneous recording.

SSMT-2000 and MT-editor software were employed primarily to convert raw time-domain data to frequency-domain data *via* fast Fourier transform and to obtain self- and mutual power spectra of the electromagnetic field during data processing. In addition, the tensor impedance was yielded by a statistically robust algorithm (Egbert and Booker., 1986; Jones et al., 1989). The phase tensor decomposition technique is used to perform the dimensionality analysis. In addition, to improve the quality of MT data, screening power spectrum and eliminating

obvious "flying points" measures were used. The apparent resistivity and the continuity of the phase curves nicely indicate deep electrical properties due to the elevated altitude and low human interference in the survey area, which makes the data quality superior for most of the survey points.

2.2. Qualitative analysis of typical measurement points

Figure 2 presents the apparent resistivity (ρ_{XY} and ρ_{YX}) and impedance phase (φ_{XY} and φ_{YX}) curve types and values for six typical measurement points in different tectonic units along the profile. Figure 2 shows that the apparent resistivity and phase curves are smooth and of high quality. Measuring points (07 and 22) are in the Lhasa terrane, 35 and 51 are in the southern Qiangtang terrane, and 65 and 80 are in the northern Qiangtang terrane. On the whole, the shape of the apparent resistivity curves is similar, and the apparent resistivity curves from high frequency to low frequency present the characteristics of high-low, which demonstrates that the shallow part of the survey area is dominated by high resistivity, while the deep part is dominated by low resistivity.

2.3. Dimensionality analysis

Before performing the inversion, it is essential to qualitatively evaluate the dimensionality (1D/2D/3D) of the MT data. The phase tensor decomposition approach is less affected by galvanic distortion caused by near-surface nonuniformity, which is widely applied to analyse regional dimensionality (Caldwell et al., 2004). The phase tensor method can be graphically represented as a series of ellipses consisting of three elements: maximum phase (φ_{max}), minimum phase (φ_{min}), and phase tensor skew angle (β). φ_{max} and φ_{min} correspond to the long and short axes of the ellipse, respectively, and their directions represent the orthogonal electrical axes, so they indicate the lateral variation in the subsurface electrical structure. The colour represented by the phase tensor skew angle (β) can be used to evaluate the dimensionality of the subsurface structure. In general, when $\beta < 3°$, it indicates that the subsurface structure is mainly one-dimensional (1D) or two-dimensional (2D), φ_{max} and φ_{min} are equal in one-dimensional conditions, and the phase tensor ellipse is circular; when $\beta > 3°$, the subsurface structure is dominated by a three-dimensional (3D) structure in isotropic settings (Booker, 2014). Figure 3 shows the phase tensor ellipses for all the measurement points along the profile at different periods. In the period range of 0.1–100 s, the phase tensor values of most measured points are narrow (less than 3°), which indicates that the shallow sedimentary structures are two dimensions or approximately one dimension. In the period from 1,000 s to 2,000 s, the phase tensor values of most survey points in the
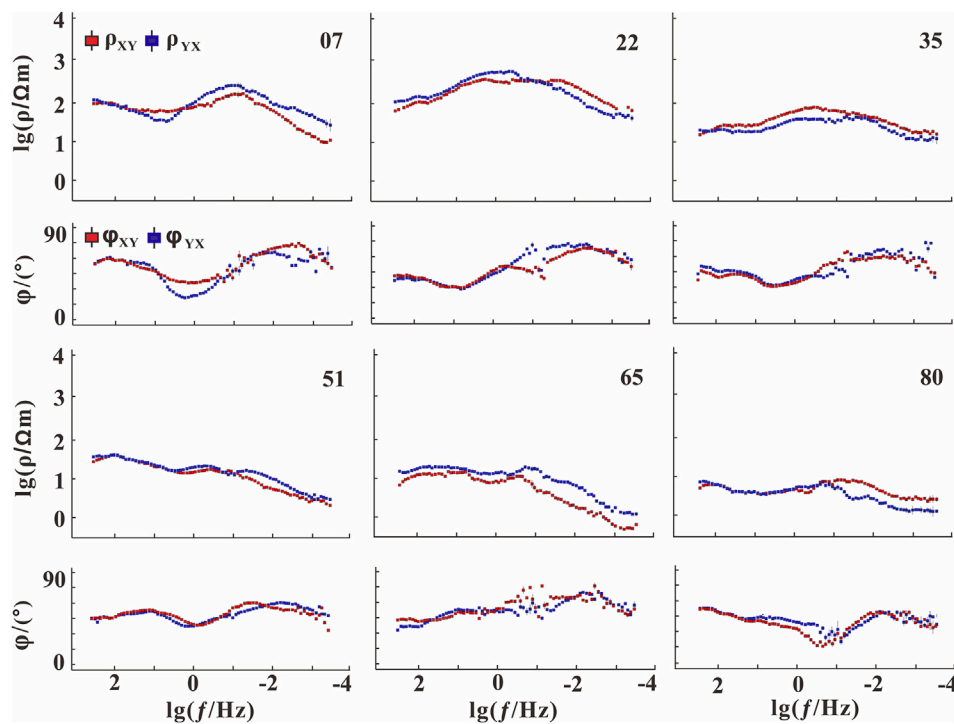
FIGURE 2
Apparent resistivity and phase curves for typical MT stations along the profile.

northern part of the Qiangtang terrane are greater than 5°. Based on the above analysis and the characteristics of MT sounding curves (Figure 2), the values of skewness essentially demonstrate that regional-scale electrical structure has two-dimensional characteristics in general. Therefore, to achieve a reliable deep electrical structure, it is reasonable to perform a 2D magnetotelluric inversion along the profile.

2.4. Strike analysis

To estimate the orientation of the deep structures in the studied region, the electrical principal axes were analysed at all measured points. Figure 3 shows the rose diagrams of the impedance tensor decomposition electrical trend in multiple frequency bands (0.1–1 s, 1–10 s, 10–100 s, 100–1,000 s) with all MT measurement points in the profile. Figure 3 shows that the orientation of the electrical principal axes is less pronounced in the high frequency band; however, it dominates in the mid-low frequency band. The optimal orientation of the electrical principal axis is 90° or 180° in the diagrams. As the uncertainty of the electrical principal axis orientation is 90°, the dominant electrical principal axis orientation may indicate the direction of the electrical structure or may correspond to the tendency. Combined

with the geological structure strike and regional fault strike, it can be judged that the overall tectonic strike of the study area is approximately NE 90°. The horizontal electric and magnetic fields are received in the north-south and east-west directions. Therefore, the tensor rotation method was used to rotate all the measurement points by 90° to attain the TM mode data with the electric field (Ex) direction perpendicular to tectonic orientation and TE mode data with the electric field direction parallel to tectonic orientation.

3 Two-dimensional (2D) inversion

We employed the WinGlink inversion module system to execute a 2D MT inversion based on a nonlinear conjugate gradient algorithm (NLCG) (Rodi and Mackie, 2001). Based on numerous inversion parameters, different polarization modes, and full-parameter joint inversion tests, two-dimensional inversion models of the profiles were finally compared and analysed, with the single TM mode being relatively reliable. 2D inversion parameters are selected as follows: the horizontal and vertical smoothness ratio α =1. The inversion data error floor was set at 10% for the apparent resistivity and 5% for the phase, and the homogeneous half-space of the initial inversion model was assigned to 100 Ω m. The
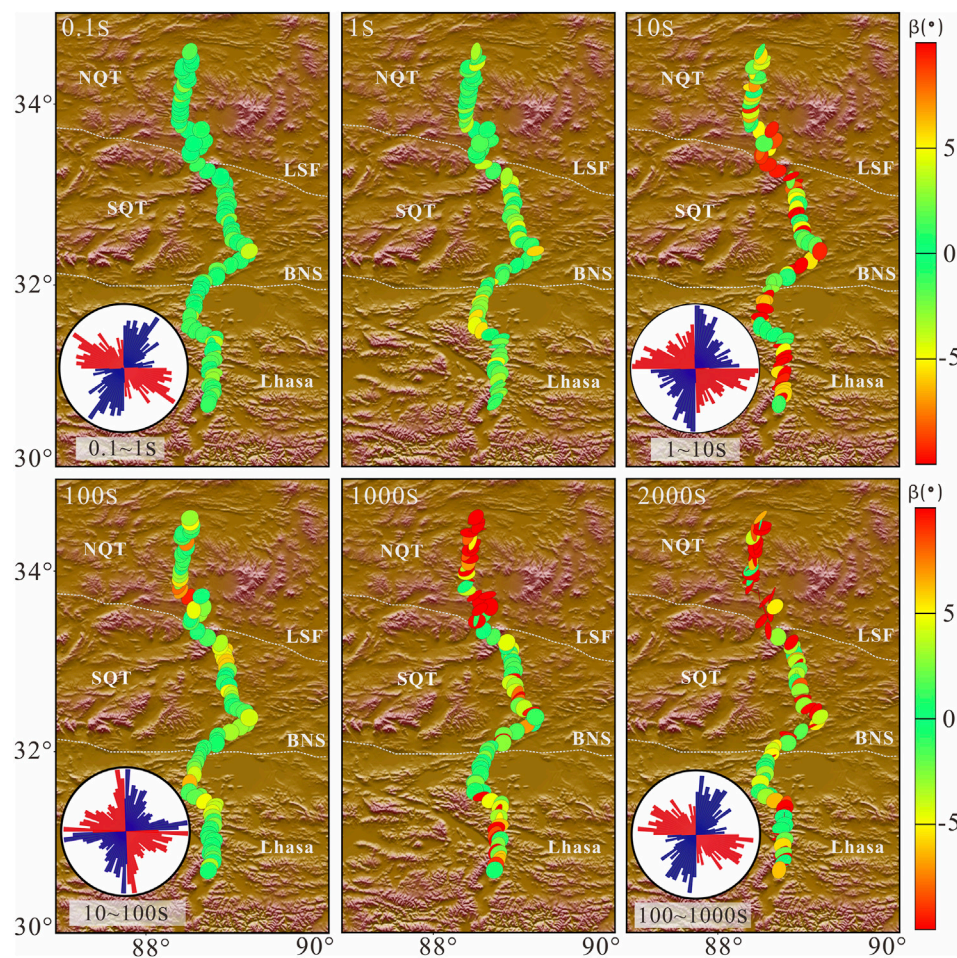
FIGURE 3
Phase tensor skew angle (β/°) for different periods along the profile and rose diagrams showing strike analysis results for each corresponding frequency band.

regularization parameter τ controls the trade-off between both model roughness and data fit. According to the calculation results, the L-curve of model roughness and data misfit (RMS) is drawn (Figure 4). Based on the L-curve analysis technique (Hansen, 1992), the optimal τ was selected. In Figure 4, when τ = 3, the preferable inversion model not only has excellent smoothness but also fits the data correctly. Finally, after 200 iterations of inversion, the preferred model was obtained with the root-mean-square misfit (RMS) of inversion Model 1.67, which demonstrates that the MT data fit the preferred model response properly, further indicating that the inversion model (Figure 6) has a certain reliability. Figure 5 shows a comparison of the apparent resistivity and impedance phases between the theoretical response data and the measured data. The results indicate that the model response data fit the measured data nicely, which also shows that the inversion model (Figure 6) is true and reliable.

4 Interpretation and discussion

4.1. Interpretation

Electrical structures imaged by 2D inversions predominantly reveal the electrical properties of the upper mantle from the surface to 100 km in the studied region. The Lhasa terrane (LS) is located in the southernmost profile, and its deep electrical structure is characterized by blocks along the profile and longitudinal stratification. The electrical property of the upper crust (0–20 km) is identified by broken resistors with a north-leaning conductor under the Gyaring co fault (GCF), which may represent the deep extension of the GCF. The first layer of high resistivity corresponds to the Cenozoic volcanic rocks that are found throughout the Lhasa terrane. Additionally, the middle-lower crust (20–71 km) is dominated by an alternating distribution of

FIGURE 4
L-curve of RMS values and roughness when Tau (τ) is changed.
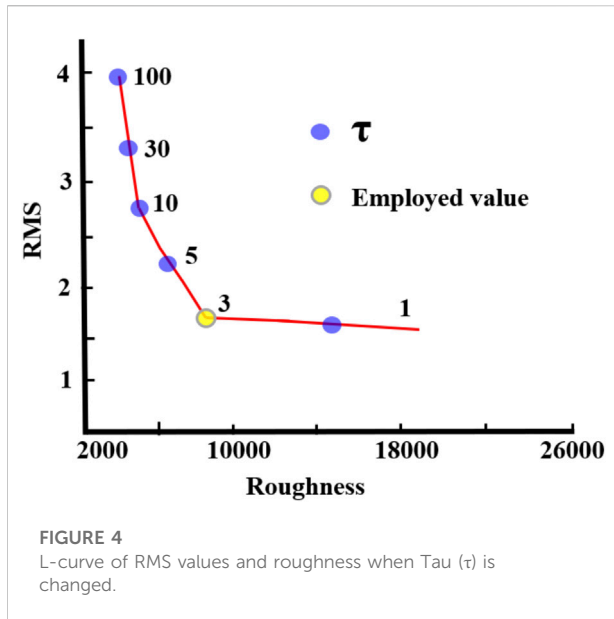
conductors and resistors marked as R1, which was attributed to the crystallization basement. The second layer with connected conductors may be caused by aqueous fluids and/or partial melting (Wei et al., 2001; Unsworth et al., 2005). The near-upright conductor (C1) extends downward from near-surface to upper mantle. The third layer (71–100 km) is characterized by a resistive upper mantle with a near-vertical conductor (C1). C1 is comparable to south-dipping fabrics (SDF) in deep seismic reflection (Figure 7).

The upper crust in the southern part of the Qiangtang terrane (SQT) remarkably manifests as a broken resistance layer with a high resistivity of approximately 1,000 Ω.m. at a depth of less than 30 km, which may be due to the widespread distribution of Mesozoic magmatic rocks in the Qiangtang terrane. In addition, the electrical properties of the mid-lower crust and upper mantle are dominated by large conductivity anomalies. Therein, a north-dipping conductor (C2) with a low resistivity of approximately 1 Ω.m. extends downward to ~100 km, which was likely due to the northward subduction of the Bangong-Nujiang Tethyan Ocean. The Bangong-Nujiang suture (BNS) is located between the SQT and LS, which appears as a distinct electrical gradient with a resistor sandwiched between two conductors (C1 and C2) in the middle-lower crust and lithospheric mantle and mainly consists of a conductor in the upper crust. The BNS exhibits a 100 km wide sutured zone in its electrical structure. Additionally, the two conductive anomaly bodies (C1 and C2) are characterized by prominent south and north dips, respectively. Likewise, the electrical characteristics of C1 and C2 are related to bidirectional reflections (SDF and NDF) in deep seismic reflection profiles (Figure 7).

The electrical characteristics in the central Qiangtang terrane (CQT) exhibit a resistive upper crust overlying conductive middle-lower crust and lithospheric mantle. The Northern Qiangtang terrane (NQT) and CQT have similar electrical characteristics in the crust and lithospheric mantle. The resistive layer was widely distributed in the upper crust of the Qiangtang terrane, corresponding to igneous rocks widely distributed in northern Tibet. Additionally, the Longmu Tso-Shuanghu fault (LSF) is located between the CQT and NQT, an anticline-shaped (C3 and C4) low-resistance band distributed from the upper crust to the upper mantle is recognized below the CQT, and a resistor (R2) is detected in the upper mantle. Compared to the conductance anomaly of the NQT, the conductance anomaly of the SQT is deeper and more developed and is associated with the subduction of the Bangong-Nujiang Tethyan Ocean during the Mesozoic and the northward subduction of the Indian lithosphere.

4.2. Discussion

4.2.1. The subduction polarity of the Bangong-Nujiang Tethyan Ocean (BTO)

A distinctive feature of the electrical structure was that two conductors (C1 and C2) with opposite dips underneath the BNS are on the lithospheric scale, which indicates the bidirectional subduction of the BTO. The BNS marked the boundary between the Lhasa and Qiangtang terranes and documented the BTO's descent and demise. Currently, there are three hypotheses for the subduction polarity of the BTO that are still under debate, namely, the northward subduction of the BTO, the southward subduction of the BTO, and the bidirectional subduction of the BTO.

Our MT imaging that two conductors (C1 and C2) mainly result from southward and northward subduction of the BTO was compatible with additional proof. Numerous primarily geochemical and geological observations have tested the possible subduction polarity of the BTO. Surface geological analysis of the Mesozoic accretionary complex (Zeng et al., 2016; Li et al., 2017) spread over the southern Qiangtang terrane and the Jurassic foreland basin found in the northern Lhasa terrane were compatible with northward subduction of the BTO (Kapp et al., 2007). Geochemical observations also reveal the presence of Mesozoic magmatic arcs in the southern Qiangtang terrane (Li et al., 2014a; Zhu et al., 2016) and ophiolitic fragments (Kapp and DeCelles, 2019) derived from northward subduction of the BTO. A similar interpretation, revealed by our MT imaging, suggests that the north-dipping conductor C2 may be associated with the northward subduction of the BTO. In addition, the Cretaceous calc-alkaline arc and the Xihu group accretionary complex (Zhu et al., 2016) distributed along the northern Lhasa terrane may reflect the southward subduction of the BTO (Li et al., 2018; Tang et al., 2020). Cretaceous calc-alkaline volcanism, whose composition
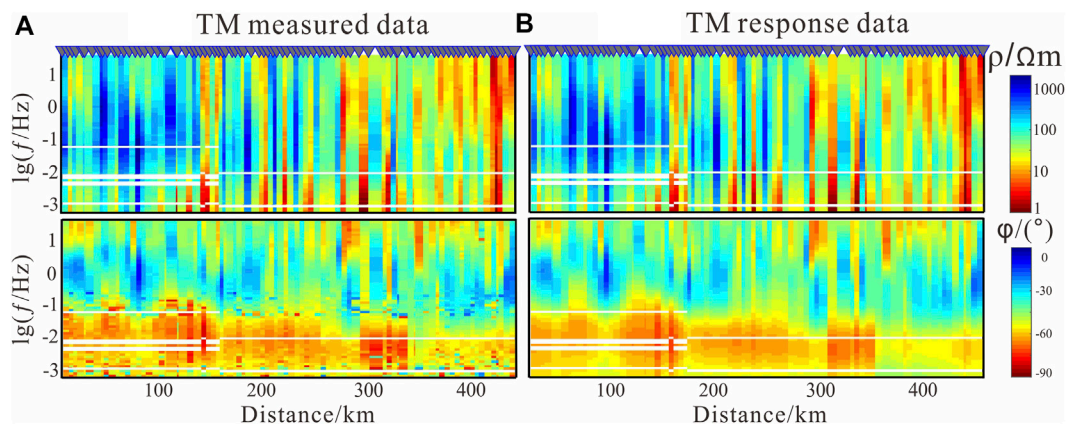
FIGURE 5
Pseudocross sections of **(A)** observed and **(B)** modelled TM data of apparent resistivity and phase.
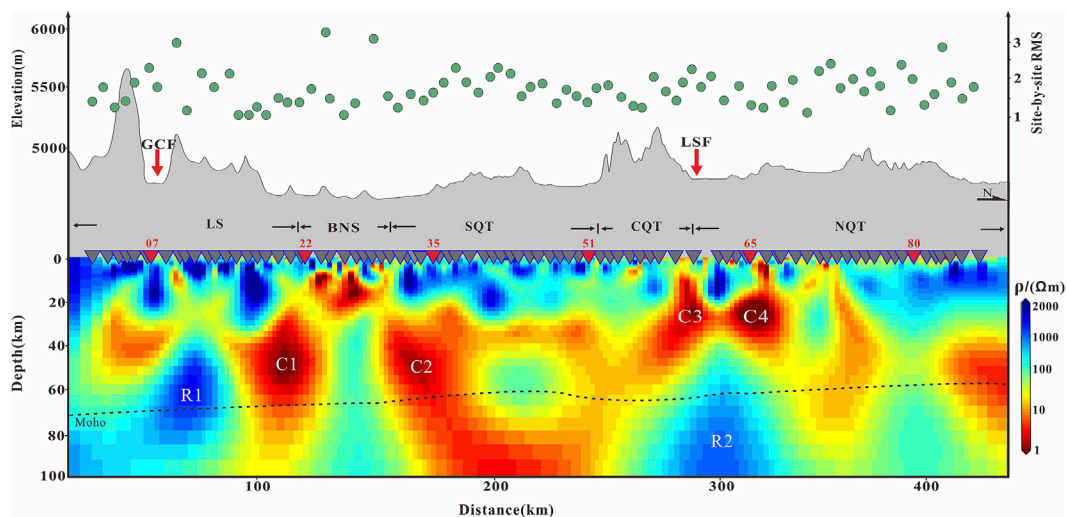
FIGURE 6
2-D electrical structure model. The green circles represent the RMS distribution. LS, Lhasa terrane; SQT, southern Qiangtang terrane; CQT, central Qiangtang terrane (central uplift zone); NQT, northern Qiangtang terrane, BNS, Bangong-Nujiang suture; LSF, Longmu Tso-Shuanghu fault; GCF, Gyaring co fault; Moho depth derived from (Gao et al., 2013; Lu et al., 2015).

ranges from medium-K to high-K (Li et al., 2018), was supposed to have undergone the break-off of the south-leaning BTO. Similarly, our MT imaging suggests that the southward-dipping conductor C1 may have resulted from the southward subduction of the BTO. Additionally, due to the lack of Cretaceous high-grade metamorphic rocks underneath the BNS, a double subduction model was supported by Zhu et al. (2016).

The above studies are mainly geochemical and geologic methods. In addition, geophysical observations constrain the deep structure of the BNS. Our MT imaging and analysis of

the conductors (C1 and C2) was also reported by previous MT research. A previous MT study demonstrated two conductors distributed on the lithospheric scale below the BNS, which are associated with the bidirectional subduction of the BTO, and the root causes may be asthenospheric upwelling, aqueous fluid and partial melting caused by the subduction of the BTO (Sheng et al., 2019). Numerous broadband passive source seismic explorations have also been carried out in the BNS (Wu et al., 2019a; Wu et al., 2019b; Nie et al., 2020). In contrast, the above studies did not focus on the subduction polarity of the BTO.
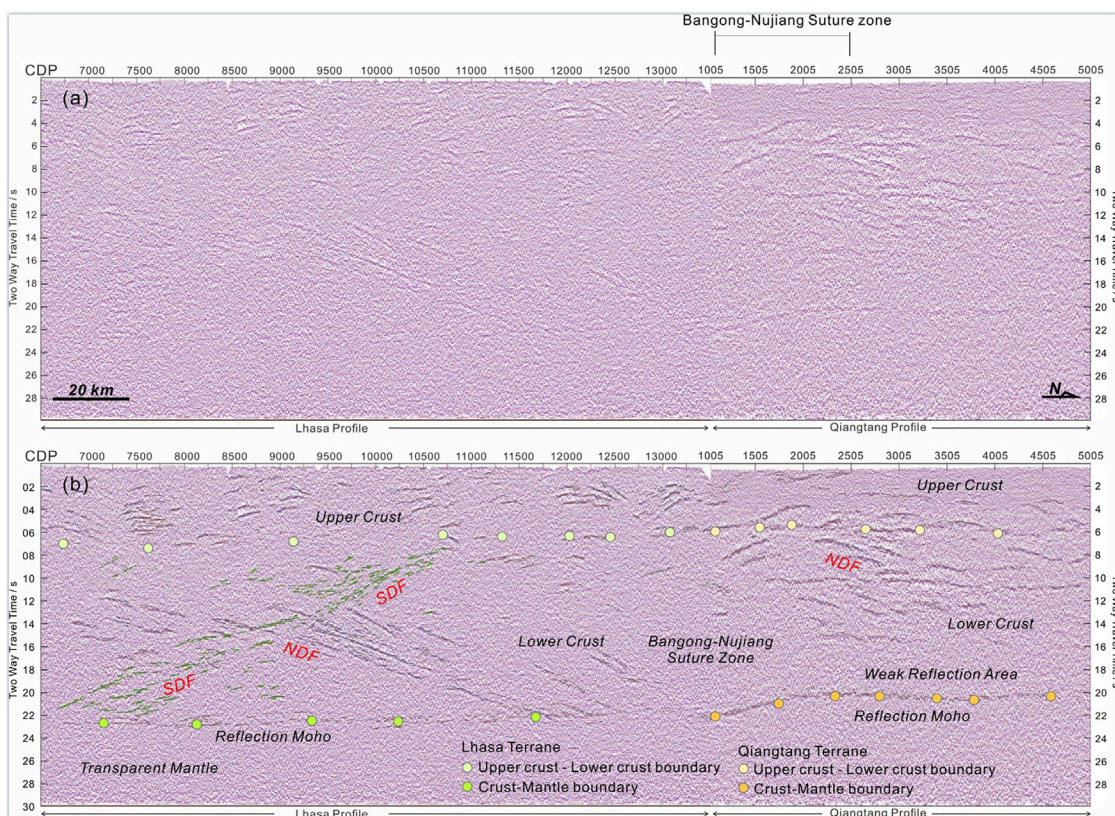
FIGURE 7
The deep seismic reflection result along the partial profile (Shi et al., 2021); **(A)**: migrated seismic reflection result **(B)**: Interpreted seismic reflection result; the Common Deep Point numbers (CDP) indicating the horizontal axis and two-way travel time indicating the vertical axis. SDF, south-dipping fabrics; NDF, north-dipping fabrics.
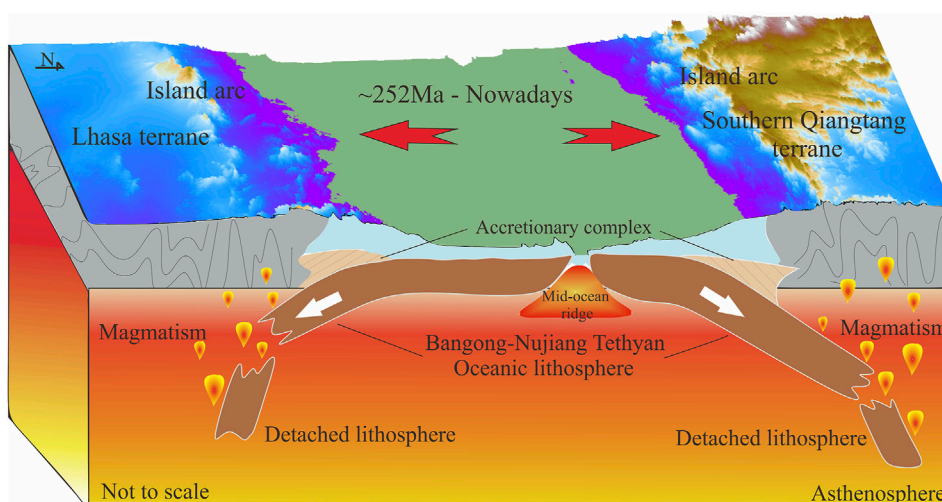
FIGURE 8
Cartoon of the bidirectional subduction of the Bangong-Nujiang Tethyan Ocean; Subduction-related accretionary complex, island arc and magmatism are also drawn.

Deep seismic reflection methods suggest that the orientation of the reflector is related to the subduction polarity. Deep seismic reflection profile data indicate that there are north-dipping reflections in the lower crust of the Qiangtang terrane, which resulted from the northward subduction of the BTO in the Mesozoic (Gao et al., 2013). In addition, seismic reflection data also discovered that there are south-dipping reflections in the middle-lower crust of the Lhasa terrane, which was attributed to the southward subduction of the BTO (Gao et al., 2016). However, reprocessed seismic reflection data led to the general notion that there are north-dipping reflections underneath the Qiangtang terrane and south-dipping reflections underneath the Lhasa terrane, which corresponds with the bidirectional subduction of the BTO (Shi et al., 2021) (Figure 7). The bidirectional reflectors are similar to our bidirectional conductors (C1 and C2). The above signatures reveal reflector structures in the crust *via* seismic reflection. More importantly, there is also a Moho constraint on the subduction polarity.

Previous studies account for the subduction polarity by means of the geometry of the Moho in additional areas (Cook et al., 1999; Ustaszewski et al., 2012; Schiffer et al., 2014). Seismic reflection exploration documented a few north-dipping Moho steps beneath the BNS (Ross et al., 2004). Similarly, the receiver function method indicated an approximately 5 km Moho offset south of the BNS (Shi et al., 2016). Additionally, wide-angle reflection observations reveal that the Moho depth shallows by ~2–3 km across the BNS (Zhao et al., 2001). A similar phenomenon was reported by seismic reflection data that recorded a decrease in the depth of the Moho (Shi et al., 2021).

Considering our MT imaging, the trace of the south-dipping conductor (C1) mainly results from the Mesozoic southward subduction of the BTO lithosphere under the Lhasa terrane, and the trace of the north-dipping conductor (C2) is likely due to the Mesozoic northward subduction of the BTO lithosphere under the Qiangtang terrane. An immediate consequence of subduction is widespread postcollisional magmatism. Additionally, lithospheric-scale conductors (C1 and C2) may have arisen from aqueous fluids and/or partial melting. The bidirectional subduction of the BTO may dehydrate and result in upwelling of the asthenosphere as the depth increases, and gravitational subsidence may trigger roll-back and break-up of the slab front, as well as delamination associated with density instabilities, which additionally leads to upwelling of the asthenospheric material. In addition, the tectonic thermal energy generated by the bidirectional subduction of the BTO leads to partial melting of the surrounding material. In summary, as demonstrated above, the BTO should have undergone bidirectional subduction.

4.2.2. The formation of a high-conductivity anomaly underneath the Qiangtang terrane

Another salient feature of the electrical structure is that a high-conductivity anticline (C3 and C4) beneath the central Qiangtang terrane is also of lithospheric scale, which is in accordance with the blueschist-bearing metamorphic belt. The electrical structure is also compatible with additional geophysical observations. A deep seismic reflection profile also revealed that an antiformal structure in the crust of the Qiangtang terrane corresponds with the central blueschist-bearing metamorphic belt (Gao et al., 2013). Similarly, the deep electrical structure of the Qiangtang terrane was also analysed by the magnetotelluric method, and the results revealed that a high-conductivity antiform at the lithospheric scale beneath the central Qiangtang terrane was remarkable (Zeng et al., 2015). In addition, the lower Q value of the upper mantle in the Qiangtang terrane (Molnar, 1988), the lower Pn wave velocity and the absence of Sn waves (Xu et al., 2011) were attributed to the low-velocity body beneath the Qiangtang terrane.

The tectonic origin of the high-conductivity anomaly beneath the Qiangtang terrane has been widely debated. There are several hypotheses for the formation of the high-conductivity anomaly. One view holds that the high conductivity underneath the Qiangtang terrane may have resulted from partial melting (Wei et al., 2001). Another point of view suggests that the high-conductivity anomaly is related to the upwelling of asthenospheric material (Unsworth et al., 2004; Wu et al., 2016; Zhu et al., 2016). Zeng et al. (2015) deems that the high-conductivity anomaly is caused by aqueous fluid and/or partial melting (Li et al., 2003). Sheng et al. (2019) delineated that the high-conductivity anomaly is due to the subduction of the Longmu Tso-Shuanghu Tethyan Ocean.

According to the geophysical and geological models given above, our MT indicates that the high-conductivity anticline (C3 and C4) in the Qiangtang terrane may be associated with aqueous fluid and/or partial melting, as well as the northward subduction of the Bangong-Nujiang Tethyan Ocean lithosphere under the SQT. In addition, the northward subduction of the BTO was heated and dehydrated, which synchronously resulted in thermal disturbance of the asthenosphere, upwelling of mantle material, and large-scale magmatic activity. A P-wave tomography study also demonstrated that a low-velocity anomaly was found in the crust of the Qiangtang terrane, which was presumed to be caused by the upwelling of mantle magma along the tectonically weak zone (Zhou and Murphy, 2005). As a result, the south-dipping conductor (C3) is likely sourced from the upwelling of postcollisional magmatism. Subsequently, gravitational drag causes the rollback and break-off of the oceanic slab, which generates an extended environment and further exacerbates the upwelling of the molten material, typically producing massive eruptions of ultrapotassic volcanic rocks. Similarly, geochemical signatures also proved that the large-scale Cenozoic ultrapotassic lavas widely developed on the surface of the Qiangtang terrane (Chung et al., 2005), which originated from the lithospheric mantle and were caused by thermal convection triggered by lithospheric subsidence (Holbig and Grove, 2008). Accordingly, the anticlinal high-conductivity configuration imaged by our MT is related to northward subduction of the BTO, aqueous fluid and/or partial melting.

5 Conclusion

In this study, we have analysed and imaged a recent high-quality magnetotelluric survey covering the junction of the northern Lhasa and Qiangtang terranes, which allows us to elaborate a geodynamical evolution model. Additionally, previous geological, geochemical, and geophysical evidence is the basis of our integrated study. Debates essentially concern three significant questions: 1) a lithospheric-scale tectonic scenario in which the Bangong-Nujiang Tethyan Ocean bidirectionally plunged under the Lhasa and Qiangtang terranes (Figure 8); 2) an anticline high-conductivity anomaly detected underneath the central Qiangtang metamorphic belt, which may be associated with aqueous fluid and/or partial melting, as well as the northward subduction of the Bangong-Nujiang Tethyan Ocean lithosphere under the Qiangtang terrane. 3) The main fault zones all show obvious high-conductivity anomalies, among which the LongmuTso-Shuanghu fault appears as an anticline-shaped conductivity anomaly.

Data availability statement

The original contributions presented in the study are included in the article/supplementary material, further inquiries can be directed to the corresponding author.

Author contributions

ZY: Methodology, Software, Formal analysis, Investigation, Validation, Visualization, Data acquisition, Writing—review and editing, Writing—original draft. HL: Methodology, Software, Formal analysis, Writing—review and editing, Resources, Funding acquisition, Project administration, Formal analysis, Validation. RG: Funding acquisition, Writing—review and editing. JH: Funding acquisition, Writing—review and editing. ZX: Methodology, Software. JK: Methodology, Software. ZS: Data

acquisition. LZ: Data acquisition, Writing—review and editing. RQ: Writing—review and editing. HL: Writing—review and editing.

Conflict of interest

The authors declare that the research was conducted in the absence of any commercial or financial relationships that could be construed as a potential conflict of interest.

Publisher's note

All claims expressed in this article are solely those of the authors and do not necessarily represent those of their affiliated organizations, or those of the publisher, the editors and the reviewers. Any product that may be evaluated in this article, or claim that may be made by its manufacturer, is not guaranteed or endorsed by the publisher.

References

Booker, J. R. (2014). The magnetotelluric phase tensor: A critical review. *Surv. Geophys.* 35, 7–40. doi:10.1007/s10712-013-9234-2

Caldwell, T. G., Bibby, H. M., and Brown, C. (2004). The magnetotelluric phase tensor. *Geophys. J. Int.* 158, 457–469. doi:10.1111/j.1365-246x.2004.02281.x

Chung, S. L., Chu, M. F., Zhang, Y. Q., Xie, Y. W., Lo, C. H., Lee, T. Y., et al. (2005). Tibetan tectonic evolution inferred from spatial and temporal variations in post-collisional magmatism. *Earth. Sci. Rev.* 68, 173–196. doi:10.1016/j.earscirev.2004.05.001

Cook, F. A., Van der Velden, A. J., Hall, K. W., and Roberts, B. J. (1999). Frozen subduction in Canada's Northwest Territories: Lithoprobe deep lithospheric reflection profiling of the Western Canadian Shield. *Tectonics* 18, 1–24. doi:10.1029/1998tc900016

Ding, L., Kapp, P., Cai, F. L., Garzione, C. N., Xiong, Z. Y., Wang, H. Q., et al. (2022). Timing and mechanisms of Tibetan Plateau uplift. *Nat. Rev. Earth Environ.* 3, 652–667. doi:10.1038/s43017-022-00318-4

Egbert, G. D., and Booker, J. R. (1986). Robust estimation of geomagnetic transfer functions. *Geophys. J. Int.* 87, 173–194. doi:10.1111/j.1365-246x.1986.tb04552.x

Fan, J. J., Li, C., Xie, C. M., Wang, M., and Chen, J. W. (2015). Petrology and U–Pb zircon geochronology of bimodal volcanic rocks from the Maierze Group, northern Tibet: Constraints on the timing of closure of the Banggong–Nujiang Ocean. *Lithos* 227, 148–160. doi:10.1016/j.lithos.2015.03.021

Gao, R., Chen, C., Lu, Z., Brown, L., Xiong, X. S., Li, W. H., et al. (2013). New constraints on crustal structure and moho topography in central Tibet revealed by SinoProbe deep seismic reflection profiling. *Tectonophysics* 606, 160–170. doi:10.1016/j.tecto.2013.08.006

Gao, R., Lu, Z. W., Klemperer, S. L., Wang, H. Y., Dong, S. W., Li, W. H., et al. (2016). Crustal-scale duplexing beneath the yarlung-zangbo suture in the Western Himalaya. *Nat. Geosci.* 9, 555–560. doi:10.1038/ngeo2730

Hansen, P. C. (1992). Analysis of discrete ill-posed problems by means of the L-curve. *SIAM Rev. Soc. Ind. Appl. Math.* 34, 561–580. doi:10.1137/1034115

He, R. Z., Liu, G. C., Golos, E., Gao, R., and Zheng, H. (2014). Isostatic gravity anomaly, lithospheric scale density structure of the northern Tibetan plateau and geodynamic causes for potassic lava eruption in Neogene. *Tectonophysics* 628, 218–227. doi:10.1016/j.tecto.2014.04.047

He, R. Z., Zhao, D. P., Gao, R., and Zheng, H. W. (2010). Tracing the Indian lithospheric mantle beneath central Tibetan Plateau using teleseismic tomography. *Tectonophysics* 491, 230–243. doi:10.1016/j.tecto.2010.03.015

Holbig, E. S., and Grove, T. L. (2008). Mantle melting beneath the Tibetan Plateau, experimental constraints on ultrapotassic magmatism. *J. Geophys. Res.* 113, B04210–B04389. doi:10.1029/2007jb005149

Hou, Z., Duan, L., Lu, Y., Zheng, Y., Zhu, D., Yang, Z., et al. (2015a). Lithospheric architecture of the Lhasa terrane and its control on ore deposits in the Himalayan-Tibetan orogen. *Econ. Geol.* 110, 1541–1575. doi:10.2113/econgeo.110.6.1541

Huang, W. C., Ni, J. F., Tilmann, F., Nelson, D., Guo, J., Zhao, W., et al. (2000). Seismic polarization anisotropy beneath the central Tibetan Plateau. *J. Geophys. Res.* 105 (B12), 27979–27989. doi:10.1029/2000JB900339

Jin, S., Sheng, Y., Comeau, M. J., Becken, M., Wei, W., Ye, G., et al. (2022). Relationship of the crustal structure, rheology, and tectonic dynamics beneath the Lhasa-Gangdese terrane (southern Tibet) based on a 3-D electrical model. *JGR. Solid Earth* 127, e2022JB024318. doi:10.1029/2022JB024318

Jones, A. G., Chave, A. D., Egbert, G., Auld, D., and Bahr, K. (1989). A comparison of techniques for magnetotelluric response function estimation. *J. Geophys. Res.* 94 (B10), 14201–14213. doi:10.1029/JB094iB10p14201

Kang, Z. Q., Xu, J. F., Wang, B. D., and Chen, J. L. (2010). Qushenla formation volcanic rocks in north Lhasa block: Products of Bangong Co-nujiang tethy's southward subduction. *Acta Petrol. Sin.* 26, 3106–3116.

Kapp, P., Decelles, P. G., Gehrels, G. E., Heizler, M., and Ding, L. (2007). Geological records of the lhasa-qiangtang and indo-asian collisions in the nima area of central Tibet. *Geol. Soc. Am. Bull.* 119, 917–933. doi:10.1130/b26033.1

Kapp, P., and DeCelles, P. G. (2019). Mesozoic-Cenozoic geological evolution of the Himalayan-Tibetan orogen and working tectonic hypotheses. *Am. J. Sci.* 319, 159–254. doi:10.2475/03.2019.01

Li, J. X., Qin, K. Z., Li, G. M., Xiao, B., Zhao, J. X., and Chen, L. (2014a). Petrogenesis of cretaceous igneous rocks from the duolong porphyry Cu-Au deposit, central Tibet: Evidence from zircon U-Pb geochronology, petrochemistry and Sr-Nd-Pb-Hf isotope characteristics. *Geol. J.* 51, 285–307. doi:10.1002/gj.2631

Li, S., Ding, L., Guilmette, C., Fu, J., Xu, Q., Yue, Y., et al. (2017). The subduction-accretion history of the bangong-nujiang ocean: Constraints from provenance and geochronology of the mesozoic strata near gaize, central Tibet. *Tectonophysics* 702, 42–60. doi:10.1016/j.tecto.2017.02.023

Li, S., Martyn, J. U., John, R. B., Wei, W., Tan, H., and Alan, G. J. (2003). Partial melt or aqueous fluid in the mid-crust of southern Tibet? Constraints from INDEPTH magnetotelluric data. *Geophys. J. Int.* 153, 289–304. doi:10.1046/j.1365-246X.2003.01850.x

Li, S. M., Wang, Q., Zhu, D. C., Stern, R. J., Cawood, P. A., Sui, Q. L., et al. (2018). One or two early Cretaceous arc systems in the Lhasa terrane, southern Tibet. *J. Geophys. Res. Solid Earth* 123, 3391–3413. doi:10.1002/2018jb015582

Liang, H. D., Jin, S., Wei, W. B., Gao, R., Ye, G. F., Zhang, L. T., et al. (2018). Lithospheric electrical structure of the middle Lhasa terrane in the south Tibetan plateau. *Tectonophysics* 731-732, 95–103. doi:10.1016/j.tecto.2018.01.020

Lu, Z., Gao, R., Li, H., Li, W., and Xiong, X. (2015). Variation of Moho depth across Bangong-Nujiang suture in central Tibet-results from deep seismic reflection data. *Int. J. Geosci.* 6, 821–830. doi:10.4236/ijg.2015.68066

Molnar, P. (1988). A review of geophysical constraints on the deep structure of the Tibetan plateau, the Himalaya and the Karakoram, and their tectonic implications. *Phil. Trans. R. Soc. Lond.* 326, 33–88.

Nie, S., Tian, X., Liang, X., Chen, Y., and Xu, T. (2020). Pn uppermost mantle tomography of central Tibet: Implication for mechanisms of N-S rifts and conjugate faults. *Tectonophysics* 788, 228499–499. doi:10.1016/j.tecto.2020.228499

Peng, Y., Yu, S., Li, S., Liu, Y., Santosh, M., Lv, P., et al. (2020). The odyssey of Tibetan plateau accretion prior to cenozoic India-asia collision: Probing the mesozoic tectonic evolution of the bangong-nujiang suture. *Earth. Sci. Rev.* 211, 103376–376. doi:10.1016/j.earscirev.2020.103376

Pullen, A., Kapp, P., Gehrels, G. E., Vervoort, J. D., and Ding, L. (2008). Triassic continental subduction in central Tibet and mediterranean-style closure of the paleo-tethys ocean. *Geol.* 36, 351–354. doi:10.1130/g24435a.1

Rodi, W., and Mackie, R. L. (2001). Nonlinear conjugate gradients algorithm for 2-D magnetotelluric inversion. *Geophysics* 66, 174–187. doi:10.1190/1.1444893

Ross, A. R., Brown, L. D., Pananont, P., Nelson, K. D., Klemperer, S., Haines, S., et al. (2004). Deep reflection surveying in central Tibet: Lower-crustal layering and crustal flow. *Geophys. J. Int.* 156, 115–128. doi:10.1111/j.1365-246x.2004.02119.x

Schiffer, C., Balling, N., Jacobsen, B. H., Stephenson, R. A., and Nielsen, S. B. (2014). Seismological evidence for a fossil subduction zone in the east Greenland Caledonides. *Geology* 42, 311–314. doi:10.1130/g35244.1

Sheng, Y., Jin, S., Wei, W., Ye, G. F., Dong, H., Zhang, L. T., et al. (2019). Lithospheric electrical structure in the central Tibetan plateau and its tectonic significance. *J. Asian Earth Sci.* 184, 103996–104013. doi:10.1016/j.jseaes.2019.103996

Shi, D. N., Zhao, W. J., Klemperer, S. L., Wu, Z. H., Mechie, J., Shi, J. Y., et al. (2016). West-east transition from underplating to steep subduction in the India-Tibet collision zone revealed by receiver function profiles. *Earth Planet. Sci. Lett.* 452, 171–177. doi:10.1016/j.epsl.2016.07.051

Shi, Z. X., Gao, R., Lu, Z. W., Li, W. H., Li, H. Q., Huang, X. F., et al. (2021). Bidirectional subduction of the Bangong-Nujiang ocean revealed by deep-crustal seismic reflection profile. *Tectonophysics* 837, 229455. doi:10.1016/j.tecto.2022.229455

Tang, Y., Zhai, Q. G., Hu, P. Y., Chung, S. L., Xiao, X. C., Wang, H. T., et al. (2020). Southward subduction of the bangong-nujiang Tethys ocean: Insights from ca. 161-129 ma arc volcanic rocks in the north of Lhasa terrane, Tibet. *Int. J. Earth Sci.* 109, 631–647. doi:10.1007/s00531-020-01823-x

Unsworth, M. J., Jones, A. G., Wei, W., Marquis, G., Gokarn, S. G., Spratt, J. E., et al. (2005). Crustal rheology of the Himalaya and southern Tibet inferred from magnetotelluric data. *Nature* 438, 78–81. doi:10.1038/nature04154

Unsworth, M., Wei, W. B., Jones, A. G., Li, S. H., Bedrosian, P., Booker, J., et al. (2004). Crustal and upper mantle structure of northern Tibet imaged with magnetotelluric data. *J. Geophys. Res.* 109 (B2), B02403. doi:10.1029/2002JB002305

Ustaszewski, K., Wu, Y. M., Suppe, J., Huang, H. H., Chang, C. H., and Carena, S. (2012). Crust-mantle boundaries in the taiwan-luzon arc-continent collision system determined from local earthquake tomography and 1D models: Implications for the mode of subduction polarity reversal. *Tectonophysics* 578, 31–49. doi:10.1016/j.tecto.2011.12.029

Wei, W. B., Unsworth, M., Jones, A., Booker, J., Tan, H. D., Nelson, D., et al. (2001). Detection of widespread fluids in the Tibetan crust by magnetotelluric studies. *Science* 292, 716–719. doi:10.1126/science.1010580

Wu, C., Tian, X., Xu, T., Liang, X., Chen, Y., Taylor, M., et al. (2019a). Deformation of crust and upper mantle in central Tibet caused by the northward subduction and slab tearing of the Indian lithosphere: New evidence based on shear wave splitting measurements. *Earth Planet. Sci. Lett.* 514, 75–83. doi:10.1016/j.epsl.2019.02.037

Wu, C., Tian, X., Xu, T., Liang, X., Chen, Y., Zhu, G., et al. (2019b). Upper-crustal anisotropy of the conjugate strike-slip fault zone in central Tibet analyzed using local earthquakes and shear-wave splitting. *Bull. Seismol. Soc. Am.* 109, 1968–1984. doi:10.1785/0120180333

Wu, H., Xie, C., Li, C., Wang, M., Fan, J., and Xu, W. (2016). Tectonic shortening and crustal thickening in subduction zones: Evidence from middle-late jurassic magmatism in southern Qiangtang, China. *Gondwana Res.* 39, 1–13. doi:10.1016/j.gr.2016.06.009

Xu, Q., Zhao, J. M., Pei, S. P., and Liu, H. B. (2011). The lithosphere asthenosphere boundary revealed by S-receiver functions from the Hi-CLIMB experiment. *Geophys. J. Int.* 187, 414–420. doi:10.1111/j.1365-246x.2011.05154.x

Xue, S., Chen, Y., Liang, H. D., Li, X., Liang, X. F., Ma, X. B., et al. (2021). Deep electrical resistivity structure across the Gyaring Co fault in central Tibet revealed by magnetotelluric data and its implication. *Tectonophysics* 809, 228835–231951. doi:10.1016/j.tecto.2021.228835

Yin, A., and Harrison, T. M. (2000). Geologic evolution of the Himalayan-Tibetan orogen. *Annu. Rev. Earth Planet. Sci.* 28, 211–280. doi:10.1146/annurev.earth.28.1.211

Zeng, M., Zhang, X., Cao, H., Ettensohn, F. R., Cheng, W., and Lang, X. (2016). Late triassic initial subduction of the bangong-nujiang ocean beneath Qiangtang revealed: Stratigraphic and geochronological evidence from gaize, Tibet. *Basin Res.* 28, 147–157. doi:10.1111/bre.12105

Zeng, S. H., Hu, X. Y., Li, J. H., Xu, S., Fang, H., and Cai, J. C. (2015). Detection of the deep crustal structure of the Qiangtang terrane using magnetotelluric imaging. *Tectonophysics* 661, 180–189. doi:10.1016/j.tecto.2015.08.038

Zhang, X. Z., Dong, Y. S., Wang, Q., Dan, W., Zhang, C., Deng, M. R., et al. (2016a). Carboniferous and Permian evolutionary records for the Paleo-Tethys Ocean constrained by newly discovered Xiangtaohu ophiolites from central Qiangtang, central Tibet. *Tectonics* 35, 1670–1686. doi:10.1002/2016TC004170

Zhao, W. J., Mechie, J., Brown, L. D., Guo, J., Haines, S., Hearn, T., et al. (2001). Crustal structure of central Tibet as derived from project INDEPTH wide-angle seismic data. *Geophys. J. Int.* 145, 486–498. doi:10.1046/j.0956-540x.2001.01402.x

Zhou, H. W., and Murphy, M. A. (2005). Tomographic evidence for wholesale underthrusting of India beneath the entire Tibetan plateau. *J. Asian Earth Sci.* 25, 445–457. doi:10.1016/j.jseaes.2004.04.007

Zhu, D. C., Li, S. M., Cawood, P. A., Wang, Q., Zhao, Z. D., Liu, S. A., et al. (2016). Assembly of the Lhasa and Qiangtang terranes in central Tibet by divergent double subduction. *Lithos* 245, 7–17. doi:10.1016/j.lithos.2015.06.023

Zhu, D. C., Zhao, Z. D., Niu, Y., Dilek, Y., Hou, Z. Q., and Mo, X. X. (2013). The origin and pre-Cenozoic evolution of the Tibetan plateau. *Gondwana Res.* 23, 1429–1454. doi:10.1016/j.gr.2012.02.002